RESEARCH ARTICLE

PHYSICS

Photonic orbital angular momentum with controllable orientation

Chenhao Wan [ID][1,2], Jian Chen[1], Andy Chong[3,4] and Qiwen Zhan[1,*]

[1]School of
Optical-Electrical and
Computer
Engineering,
University of Shanghai
for Science and
Technology, Shanghai
200093, China;
[2]School of Optical and
Electronic Information,
Huazhong University
of Science and
Technology, Wuhan
430074, China;
[3]Department of
Electro-Optics and
Photonics, University
of Dayton, Dayton, OH
45469, USA and
[4]Department of
Physics, University of
Dayton, Dayton, OH
45469, USA

*Corresponding
author. E-mail:
qwzhan@usst.edu.cn

ABSTRACT

Vortices are whirling disturbances, commonly found in nature, ranging from tremendously small scales in Bose-Einstein condensations to cosmologically colossal scales in spiral galaxies. An optical vortex, generally associated with a spiral phase, can carry orbital angular momentum (OAM). The optical OAM can either be in the longitudinal direction if the spiral phase twists in the spatial domain or in the transverse direction if the phase rotates in the spatiotemporal domain. In this article, we demonstrate the intersection of spatiotemporal vortices and spatial vortices in a wave packet. As a result of this intersection, the wave packet hosts a tilted OAM that provides an additional degree of freedom to the applications that harness the OAM of photons.

Keywords: orbital angular momentum, spatiotemporal vortex, spatial vortex, spiral phase

INTRODUCTION

Vortices, ubiquitous in nature, are circulating disturbances of liquid, gas or other media. They have been found in turbulent water, circulating air around wing tips, swirling galaxies and optics as well [1]. Optical vortices are generally associated with a spiral wavefront with phase singularities of zero intensity. The twisted wavefront gives rise to an azimuthal component of Poynting vector that contributes to an integrated orbital angular momentum (OAM) pointing along the beam axis. Each photon carries an OAM of $l\hbar$ where $\hbar$ is the reduced Planck's constant and l is an integer, generally referred to as the topological charge [2]. The connection of vortex beams with optical OAM has spurred substantial theoretical and experimental research and found a wealth of applications in both classical and quantum optics [3–10].

Recent theoretical studies manifest that optical OAM does not have to be longitudinal but can be tilted to the optical axis [11,12]. The tilted OAM could be realized with a fast-moving observer close to the speed of light. Experimental progress has shown that a small fraction of optical energy can circulate in a spatiotemporal plane in a non-linear interaction of an extremely high-power laser pulse and air [13]. Contrary to the longitudinal OAM that is associated with a spiral phase in the spatial domain,

the transverse OAM roots in a spiral phase in the spatiotemporal domain that rotates around an axis perpendicular to the propagation direction. Although experimentally explored, it is still a challenging task to control and manipulate a spiral phase with circulating Poynting vector in a spatiotemporal plane in a linear manner. The difficulty has recently been overcome by forming a spiral phase in the spatial frequency–temporal frequency domain and retaining the spiral phase in the spatiotemporal domain through a two-dimensional spatiotemporal Fourier transform [14–16].

The intersection of spatial vortices has been reported in literature [17]. However, the interacting dynamics stay at the intersection point and do not travel with the beam. In this work, we experimentally demonstrate the intersection of spatiotemporal vortices and spatial vortices in an optical wave packet. The wave packet contains both screw and edge dislocations in phase. The intersection of two distinct types of optical vortices reveals interesting three-dimensional energy flow that travels at the speed of light. The combination of transverse OAM carried by spatiotemporal vortices and longitudinal OAM carried by spatial vortices gives rise to a tilted OAM with respect to the optical axis. The average three-dimensional OAM per photon remain unchanged

after propagation in free space. The tilted OAM is fully controllable in value and orientation, through the topological charges of the two types of vortices. Since OAM plays an important role in light–matter interactions, the tilted OAM could be used, for example, to create optical spanners in arbitrary three-dimensional orientation with controllable torque. It can also be employed to provide an additional degree of freedom of optical OAM for applications such as optical tweezing, spin-orbit angular momentum coupling and quantum communications. Furthermore, the platform to achieve tilted OAM could possibly be utilized as a laboratory tool to simulate relativistic effects as analyzed in [11].

RESULTS

A wave packet is assumed to propagate in the z direction with a vector potential A polarized in the x direction:

$$A = u(x, y, z')e^{ikz'}x, \tag{1}$$

where x is the unit vector in the x direction, z is the propagation direction, z' is the local frame coordinate given by $z' = z - ct$, c is the speed of light in vacuum and k is the wave number. $u(x, y, z')$ is a complex scalar function describing the field distribution under paraxial approximation. A spatiotemporal vortex of topological charge l_1 and a spatial vortex of topological charge l_2 are both embedded within the wave packet. The complex scalar function u is therefore given by

$$u(x, y, z') = \left(\frac{x}{w_x} \pm i\,\text{sgn}\,(l_1)\frac{y}{w_y}\right)^{|l_1|}$$

$$\times \left(\frac{x}{w_x} \pm i\,\text{sgn}\,(l_2)\frac{z'}{w_{z'}}\right)^{|l_2|}$$

$$\times exp\left\{-\left[\left(\frac{x}{w_x}\right)^2 + \left(\frac{y}{w_y}\right)^2\right.\right.$$

$$\left.\left. + \left(\frac{z'}{w_{z'}}\right)^2\right]\right\}, \tag{2}$$

where w_x, w_y and $w_{z'}$ are the pulse dimensions along the x, y and z' directions, respectively. Here the intensity distributions are assumed to be Gaussian in all three dimensions. The linear momentum density g is the time average of the real part of $\varepsilon_0(E \times B)$ where E is the electric field, B is the magnetic field and ε_0 is the permittivity in vacuum. Following the Lorentz gauge, the linear momen-

tum density g is expressed in terms of the complex scalar function u [18]:

$$g = \frac{\varepsilon_0}{2}\left(E^* \times B + E \times B^*\right)$$

$$= \frac{\varepsilon_0}{2}\left(c\frac{\partial u^*}{\partial x}\frac{\partial u}{\partial z'} + c\frac{\partial u}{\partial x}\frac{\partial u^*}{\partial z'}\right.$$

$$\left. + i\omega u\frac{\partial u^*}{\partial x} - i\omega u^*\frac{\partial u}{\partial x}\right)x$$

$$+ \frac{\varepsilon_0}{2}\left(-i\omega u^*\frac{\partial u}{\partial y} + i\omega u\frac{\partial u^*}{\partial y}\right)y$$

$$+ \frac{\varepsilon_0}{2}\left(-i\omega u^*\frac{\partial u}{\partial z'} + i\omega u\frac{\partial u^*}{\partial z'} + 2\omega k|u|^2\right)z', \tag{3}$$

where $*$ denotes complex conjugate, y is the unit vector in the y direction and z' is the unit vector in the z' direction. The angular momentum density is given by the cross product of the position vector r with the linear momentum density g:

$$r \times g = \frac{\varepsilon_0}{2}\left[y\left(-i\omega u^*\frac{\partial u}{\partial z'} + i\omega u\frac{\partial u^*}{\partial z'}\right.\right.$$

$$\left. + 2\omega k|u|^2\right)$$

$$\left. - z'\left(-i\omega u^*\frac{\partial u}{\partial y} + i\omega u\frac{\partial u^*}{\partial y}\right)\right]x$$

$$+ \frac{\varepsilon_0}{2}\left[z'\left(c\frac{\partial u^*}{\partial x}\frac{\partial u}{\partial z'} + c\frac{\partial u}{\partial x}\frac{\partial u^*}{\partial z'}\right.\right.$$

$$\left. + i\omega u\frac{\partial u^*}{\partial x} - i\omega u^*\frac{\partial u}{\partial x}\right)$$

$$\left. - x\left(-i\omega u^*\frac{\partial u}{\partial z'} + i\omega u\frac{\partial u^*}{\partial z'}\right.\right.$$

$$\left. + 2\omega k|u|^2\right)\right]y$$

$$+ \frac{\varepsilon_0}{2}\left[x\left(-i\omega u^*\frac{\partial u}{\partial y} + i\omega u\frac{\partial u^*}{\partial y}\right)\right.$$

$$\left. - y\left(c\frac{\partial u^*}{\partial x}\frac{\partial u}{\partial z'} + c\frac{\partial u}{\partial x}\frac{\partial u^*}{\partial z'}\right.\right.$$

$$\left. + i\omega u\frac{\partial u^*}{\partial x} - i\omega u^*\frac{\partial u}{\partial x}\right)\right]z'. \tag{4}$$

The average OAM per photon within the wave packet can be derived through a volume integral:

$$OAM/photon = \frac{\int_{-\infty}^{\infty} r \times g\,dV}{\varepsilon_0\omega^2\int_{-\infty}^{\infty}|u|^2dV}h\upsilon. \tag{5}$$
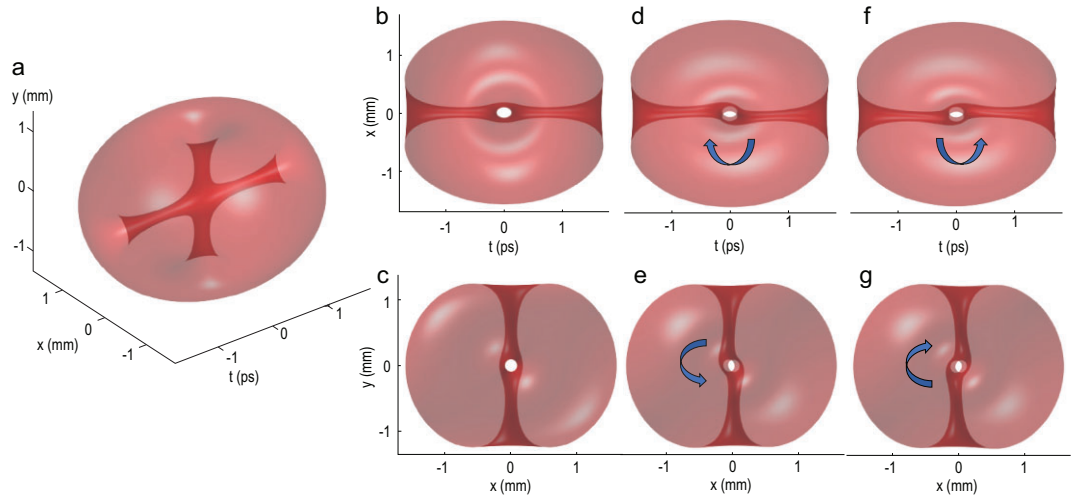
Figure 1. Simulated three-dimensional iso-intensity profiles of a wave packet with collided spatiotemporal and spatial vortices. Normalized symmetric intensity distribution and unitary topological charge are assumed. The isovalue is set to 0.02, and 96.8% of the energy of the wave packet is contained in the isosurface. Fresnel diffraction theory is used for propagation of 12 cm. (a–c) A generated wave packet with collided vortices before propagation. (d and e) A generated wave packet with collided vortices after propagation. The topological charges of the spatiotemporal vortex and spatial vortex are both +1. (f and g) A generated wave packet with collided vortices after propagation. The topological charges of the spatiotemporal vortex and spatial vortex are both −1.

The average OAM per photon is a vector that has three components pointing to the x, y and z' directions, respectively. Based on equations (2) to (5), the x, y and z' components of the OAM per photon are derived analytically. For example, if $l_1 = 3$ and $l_2 = 2$, the x, y and z' components of the OAM per photon are calculated to be 0, $\frac{2(34w_x^2 + 7w_{z'}^2)}{41w_x w_{z'}}\hbar$ and $\frac{3(65w_x^2 + 17w_y^2)}{82w_x w_y}\hbar$, respectively. Therefore, the OAM per photon within the wave packet is $\frac{1}{82}\sqrt{27506 + w_x^2(\frac{38025}{w_y^2} + \frac{18496}{w_{z'}^2}) + \frac{2601w_y^2 + 784w_{z'}^2}{w_x^2}}\hbar$ pointing in the direction of θ degrees with respect to the -y axis in the y-z' plane, where $\theta = \tan^{-1}(\frac{195w_x^2 w_{z'} + 51w_y^2 w_{z'}}{136w_x^2 w_y + 28w_y w_{z'}^2})$. Particularly, if w_x, w_y and $w_{z'}$ are of equal length, the x, y and z' components of the OAM are 0, $2\hbar$ and $3\hbar$ as expected. The theoretical analysis clarifies the fact that an average three-dimensionally oriented OAM can indeed be obtained in a non-relativistic way through the intersection of a spatiotemporal vortex and a spatial vortex within one wave packet. The associated topological charges as well as the pulse dimensions play an important role in tuning the value and three-dimensional orientation of the tilted OAM.

Figure 1a shows simulated three-dimensional iso-intensity profiles of a wave packet with intersected spatiotemporal and spatial vortices. The intensity profiles are assumed to be Gaussian, of equal length in all three directions. The topological charges of both vortices are assumed to be 1 (equation (2)). The spatiotemporal vortex twists in the x–t plane and forms a tunnel in the y direction (dark strip in Fig. 1b); the spatial vortex rotates in the x–y plane and forms a tunnel in the t direction (dark strip in Fig. 1c). After free-space propagation, the diffraction effect causes an interesting twist of the two tunnels, which can be understood as the consequence of the intersection of perpendicular vortices, at the intersection. A spatial vortex tunnel is twisted clockwise in the x–t plane by a spatiotemporal vortex of topological charge 1 (Fig. 1d). A spatiotemporal vortex tunnel is twisted counterclockwise in the x–y plane by a spatial vortex of topological 1 (Fig. 1e). Figure 1f and g shows different twisting directions because the topological charges of both vortices are changed to −1.

Figure 2a–f shows the experimental data of a generated wave packet that hosts the intersection of a spatiotemporal vortex of topological charge 1 and a spatial vortex of topological charge 1. The details of the experimental setup can be found in the supplementary information. Figure 2a–d displays four typical slices of interference images in the x–y plane of the wave packet with the reference pulse. The positions of these slices are marked in Fig. 2e. The fringe patterns in Fig. 2a are dominantly influenced by the spatial vortex because the slicing position is far from the core of the spatiotemporal vortex. The most
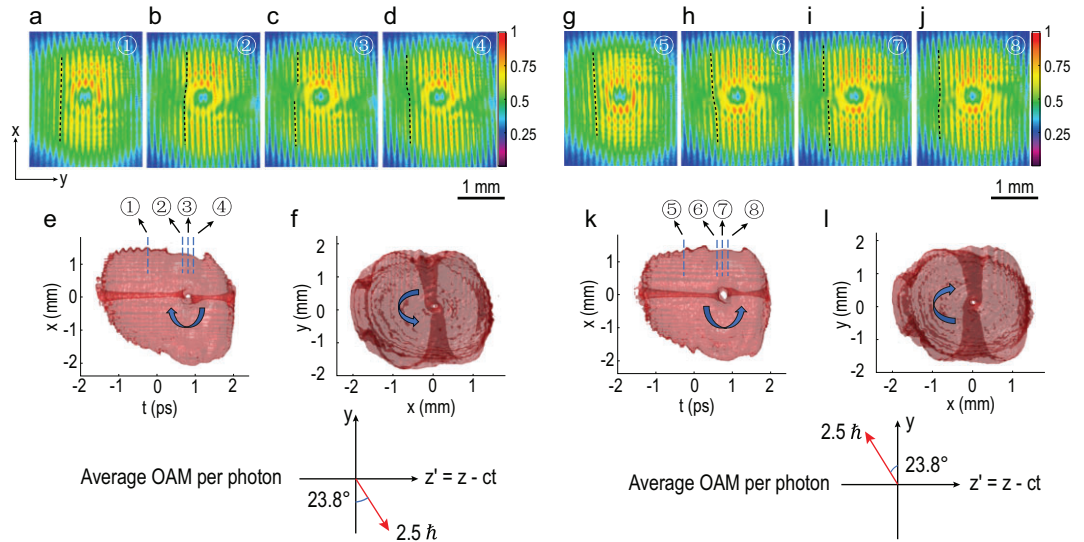
Figure 2. The intersection of a spatiotemporal vortex with a spatial vortex. (a–d) The topological charge of the spatiotemporal vortex and the spatial vortex are both 1. Interference fringe patterns of the reference pulse with the chirped wave packet at various positions. Black dashed lines mark the bending directions of fringes. (e and f) Three-dimensional intensity reconstruction of the chirped wave packet showing the intersection of a spatiotemporal vortex and a spatial vortex from different views. 91.0% of the energy of the wave packet is contained in the isosurface. Temporal separations between slices 1, 2, 3 and 4 are 1 ps, 83 fs and 83 fs, respectively. (g–j) The topological charge of the spatiotemporal vortex and the spatial vortex are both −1. Interference fringe patterns of the reference pulse with the chirped wave packet at various positions. (k and l) Three-dimensional intensity reconstruction of the chirped wave packet showing the intersection of a spatiotemporal vortex and a spatial vortex from different views. 89.8% of the energy of the wave packet is contained in the isosurface. Temporal separations between slices 1, 2, 3 and 4 are 1 ps, 83 fs and 83 fs, respectively.

noticeable feature is a fork-like pattern pointing downwards at the center that represents a spatial vortex of topological charge 1. As the reference pulse approaches the intersection center, the effect of the spatiotemporal vortex becomes more obvious. In Fig. 2b, the upper half of peripheral fringes starts to bend to the right indicating an increasing phase shift between the upper and lower parts of the wave packet. Bending fringes is a salient feature of a spatiotemporal vortex. Continued in Fig. 2c, the upper and lower peripheral fringes have a π phase difference. The dark fringes in the upper half are aligned with the bright fringes in the lower half. In Fig. 2d, the bending direction of peripheral fringes is switched. Slicing through the chirped wave packet from head to tail, the upper and lower peripheral fringes complete a 0 to π and π to 0 phase shift. The peripheral areas of fringe patterns in Fig. 2b–d have smaller spatial spiral phase gradient than the central areas. Therefore, the peripheral fringes mainly show the feature of a spatiotemporal vortex of topological charge 1. The central area of Fig. 2b–d is the intersection of the spatiotemporal vortex and the spatial vortex. The interaction of the two vortices is most intense in the central region and the features of both vortices are combined.

Extracting the optical field information from slices of fringes, the three-dimensional intensity distribution of the wave packet can be reconstructed [19–21]. Figure 2e and f shows the wave packet from different views. In Fig. 2e, a vortex core appearing as a tunnel resulting from spatiotemporal phase singularity is clearly displayed. The spatiotemporal vortex tunnel penetrates through the wave packet along the y direction. In Fig. 2f, the spatial phase singularities result in a spatial vortex tunnel that penetrates all the way from head to tail of the wave packet. The spatiotemporal vortex tunnel is twisted clockwise at the core of the intersection of the two vortices. The spatial vortex tunnel, not surprisingly, is also twisted by the spatiotemporal vortex. Based on equation (5), the average OAM per photon of the wave packet is calculated to be 2.5 $\hbar$ pointing in the direction of 23.8 degrees with respect to the $-y$ axis in the y–z' plane. Numerical simulation results show that the OAM of the wave packet is conserved during free-space propagation.

Figure 2g–l shows the intersection of a spatiotemporal vortex of topological charge −1 and a spatial vortex of topological charge −1. Figure 2g shows an interference pattern that is sliced far away
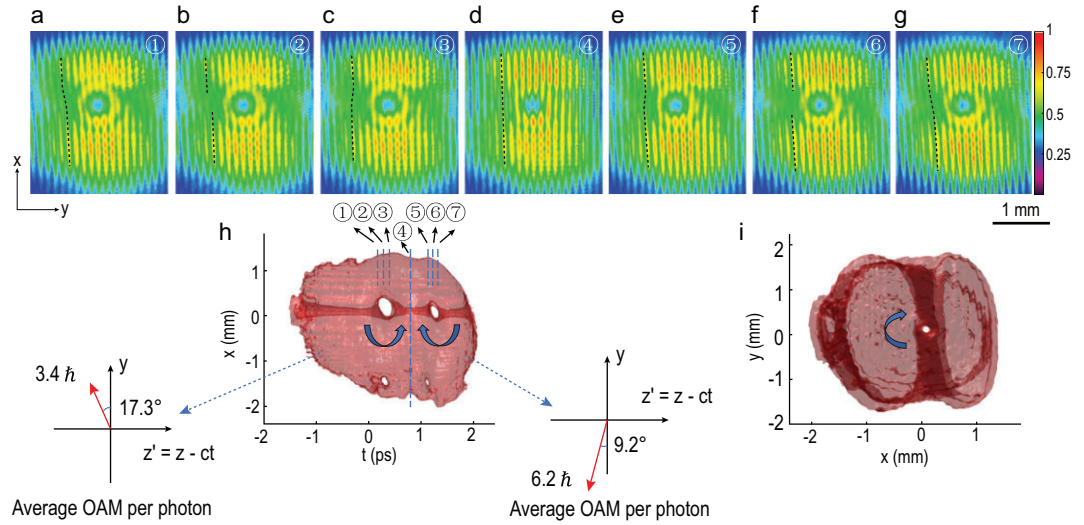
Figure 3. The intersection of two spatiotemporal vortices of topological charge −1 and 1 respectively with a spatial vortex of topological charge −1. (a–g) Interference fringe patterns of the reference pulse with the chirped wave packet at various positions. Black dashed lines mark the bending directions of fringes. (h and i) Three-dimensional intensity reconstruction of the chirped wave packet showing the intersection of two spatiotemporal vortices and a spatial vortex from different views. 88.0% of the energy of the wave packet is contained in the isosurface. Temporal separations between slices 1–7 are 83 fs, 83 fs, 383 fs, 383 fs, 83 fs and 83 fs, respectively.

from the intersection center. The spatial vortex feature is overwhelmed and a fork-like pattern pointing upwards is shown at the center of the image. The change in the pointing direction of the fork-like pattern is due to the fact that the topological charge of the spatial vortex is changed to −1. In Fig. 2h–j, the peripheral fringes display the features of a spatiotemporal vortex. Since the sign of topological charge of the spatiotemporal vortex is reversed, the upper half of peripheral fringes first bends to the left as shown in Fig. 2h until a π phase shift is accomplished as shown in Fig. 2i, and then bends to the right as shown in Fig. 2j. Figure 2k and l shows the three-dimensional intensity reconstruction of the wave packet. The spatiotemporal vortex tunnel and the spatial vortex tunnel are both twisted at the intersection. The twisting direction, however, is reversed compared to Fig. 2e and f because of the flipping of the sign of topological charge of both the spatiotemporal vortex and the spatial vortex. The average OAM per photon of the wave packet is calculated to be 2.5 $\hbar$ pointing in the direction of 23.8 degrees with respect to the *y* axis in the *y*–*z'* plane.

The experimental demonstration shown in Fig. 3 is the intersection of two spatiotemporal vortices of topological charge −1 and 1 respectively with a spatial vortex of topological charge −1 in the same wave packet. Figure 3a–g shows seven slices of interference fringe patterns. The locations of these slices are marked in Fig. 3h. Figure 3a–c shows the interfer-

ence patterns as the reference pulse slices through the intersection of the first spatiotemporal vortex with the spatial vortex. The upper half of peripheral fringes first bends to the left, then bends to the right after the π phase shift location. The first spatiotemporal vortex is therefore of topological charge −1 as also supported by the vortex tunnel twisting direction shown in Fig. 3h. Figure 3d shows a slice between the two intersections where the spatial vortex plays a dominant role over the spatiotemporal vortices. Consequently, the most noticeable feature is a fork-like pattern pointing upwards at the center. Figure 3e–g displays the interference patterns around the second intersection. The second spatiotemporal vortex has a topological charge 1 that results in a different bending sequence shown in Fig. 3e–g and an opposite twisting direction shown in Fig. 3h. This is the first experimental demonstration of the generation of an ultrafast wave packet embedded with multiple optical vortices with individually tunable orientation. The average OAM per photon of the wave packet in the head is estimated to be 3.4 $\hbar$ pointing in the direction of 17.3 degrees with respect to the *y* axis in the *y*–*z'* plane; the average OAM of the wave packet in the tail is estimated to be 6.2 $\hbar$ pointing in the direction of 9.2 degrees with respect to the −*y* axis in the *y*–*z'* plane. In this particular example, the two vortices with different OAM orientations are temporally separated by ∼1 ps. With shorter pulses, more OAM vortices with temporal

separation <100 fs packed within one wave packet can be expected.

CONCLUSION

In summary, we report the first experimental demonstration of the intersection of spatiotemporal vortices and spatial vortices. The twisting of vortex tunnels reveals the three-dimensional characteristics of optical vortices. The spatial vortex generates a longitudinal optical OAM whereas the spatiotemporal vortex provides a transverse OAM. In the intersection region where the two types of vortices interact most intensely, the vortex tunnels of both types of vortices are intertwined and twisted, indicating a complex three-dimensional spiral phase structure. The associated OAM with the three-dimensional spiral phase structure is tilted with respect to the optical axis. The OAM carried by the wave packet consists of a longitudinal component and a transverse component that can be controlled individually through their corresponding topological charges. The average three-dimensional OAM per photon contained in the wave packet remains unchanged after propagation in free space. The tilted angle of the OAM provides a new degree of freedom that could possibly be used in optical tweezing, spin-orbit angular momentum coupling and quantum communications. The first theoretical prediction on tilted OAM originates from an ordinary optical vortex with a fast-moving observer or source [11]. The experimental demonstration in this article provides a non-relativistic way to generate tilted OAM. The platform, therefore, could potentially be utilized for simulating relativistic effects as well.

SUPPLEMENTARY DATA

Supplementary data are available at *NSR* online.

AUTHOR CONTRIBUTIONS

A.C. and C.W. proposed the original idea and performed all experiments and theoretical analysis. J.C. contributed in developing the measurement method. Q.Z. guided the theoretical analysis and supervised the project. All authors contributed to writing the manuscript.

Conflict of interest statement. None declared.

REFERENCES

1. Gbur GJ. *Singular Optics*. Florida: CRC Press, 2016.
2. Allen L, Beijersbergen MW and Spreeuw RJC *et al*. Orbital angular momentum of light and the transformation of Laguerre–Gaussian laser modes. *Phys Rev A* 1992; **45**: 8185–9.
3. Cai X, Wang J and Strain MJ *et al*. Integrated compact optical vortex beam emitters. *Science* 2012; **338**: 363–6.
4. Pu M, Li X and Ma X *et al*. Catenary optics for achromatic generation of perfect optical angular momentum. *Sci Adv* 2015; **1**: e1500396.
5. Guo Y, Pu M and Zhao Z *et al*. Merging geometric phase and plasmon retardation phase in continuously shaped metasurfaces for arbitrary orbital angular momentum generation. *ACS Photon* 2016; **3**: 2022–9.
6. Pu M, Guo Y and Li X *et al*. Revisitation of extraordinary Young's interference: from catenary optical fields to spin-orbit interaction in metasurfaces. *ACS Photon* 2018; **5**: 3198–204.
7. Forbes A, Oliveira M and Dennis MR. Structured light. *Nat Photon* 2021; **15**: 253–62.
8. Forbes A and Nape I. Quantum mechanics with patterns of light: progress in high dimensional and multidimensional entanglement with structured light. *AVS Quantum Sci* 2019; **1**: 011701.
9. Padgett M. Orbital angular momentum 25 years on. *Opt Express* 2017; **25**: 11265–74.
10. Shen Y, Wang X and Xie Z *et al*. Optical vortices 30 years on: OAM manipulation from topological charge to multiple singularities. *Light Sci Appl* 2019; **8**: 1–29.
11. Bliokh KY and Nori F. Spatiotemporal vortex beams and angular momentum. *Phys Rev A* 2012; **86**: 033824.
12. Bliokh K. Spatiotemporal vortex pulses: angular momenta and spin-orbit interaction. *Phys Rev Lett* 2021; **126**: 243601.
13. Jhajj N, Larkin I and Rosenthal EW *et al*. Spatiotemporal optical vortices. *Phys Rev X* 2016; **6**: 031037.
14. Chong A, Wan C and Chen J *et al*. Generation of spatiotemporal optical vortices with controllable transverse orbital angular momentum. *Nat Photon* 2020; **14**: 350–4.
15. Hancock SW, Zahedpour S and Goffin A *et al*. Free-space propagation of spatiotemporal optical vortices. *Optica* 2019; **6**: 1547–53.
16. Wan C, Chen J and Chong A *et al*. Generation of ultrafast spatiotemporal wave packet embedded with time-varying orbital angular momentum. *Sci Bull* 2020; **65**: 1334–6.
17. Rosales-Guzmán C, Mazilu M and Baumgartl J *et al*. Collision of propagating vortices embedded within airy beams. *J Opt* 2013; **15**: 044001.

18. Lotti A, Couairon A and Faccio D *et al*. Energy-flux characterization of conical and space-time coupled wave packets. *Phys Rev A* 2010; **81**: 023810.

19. Li Y and Lewellen JW. Generating a quasiellipsoidal electron beam by 3D laser-pulse shaping. *Phys Rev Lett* 2008; **100**: 074801.

20. Li H, Bazarov IV and Dunham BM *et al*. Three-dimensional laser pulse intensity diagnostic for photoinjectors. *Phys Rev ST Accel Beams* 2011; **14**: 112802.

21. Chen J, Lu K and Cao Q *et al*. Automated close-loop system for three-dimensional characterization of spatiotemporal optical vortex. *Front Phys* 2021; **9**: 633922.